MITSUBISHI ELECTRIC RESEARCH LABORATORIES
http://www.merl.com

Outdoor-to-Indoor Office MIMO Measurements and Analysis at 5.2 GHz

Shurjeel Wyne, Andreas Molisch, Peter Almers, Gunnar Eriksson, Johan Karedal, Fredrik Tufvesson

TR2008-048 August 2008

Abstract

The outdoor-to-indoor wireless propagation channel is of interest for cellular and wireless local area network applications. This paper presents the measurement results and analysis based on our multiple-input-multiple-output (MIMO) measurement campaign, which is one of the first to characterize the outdoor-to-indoor channel. The measurements were performed at 5.2 GHz; the receiver was placed indoors at 53 different locations in an office building, and the transmitter was placed at three "base stations" positions on a nearby rooftop. We report on the root-mean-square (RMS) angular spread, building penetration, and other statistical parameters that characterize the channel. Our analysis is focused on three MIMO channel assumptions often used in stochastic models. 1) It is commonly assumed that the channel matrix can be represented as a sum of a line-of-sight (LOS) contribution and a zero-mean complex Gaussian distribution. Our investigation shows that this model does not adequately represent our measurement data. 2) It is often assumed that the Rician K-factor is equal to the power ratio of the LOS component and the other multipath components (MPCs). We show that this is not the case, and we highlight the difference between the Rician K-factor often associated with LOS channels and a similar power ratio for the estimated LOS MPC. 3) A widespread assumption is that the full correlation matrix of the channel can be decomposed into a Kronecker product of the correlation matrices at the transmit and receive array. Our investigations show that the direction-of-arrival (DOA) spectrum noticeably depends on the direction-of-departure (DOD); therefore, the Kronecker model is not applicable, and models with less-restrictive assumptions on the channel, e.g., the Weichselberger model or the full correlation model, should be used.

IEEE Transactions on Vehicular Technology

This work may not be copied or reproduced in whole or in part for any commercial purpose. Permission to copy in whole or in part without payment of fee is granted for nonprofit educational and research purposes provided that all such whole or partial copies include the following: a notice that such copying is by permission of Mitsubishi Electric Research Laboratories, Inc.; an acknowledgment of the authors and individual contributions to the work; and all applicable portions of the copyright notice. Copying, reproduction, or republishing for any other purpose shall require a license with payment of fee to Mitsubishi Electric Research Laboratories, Inc. All rights reserved.

Copyright © Mitsubishi Electric Research Laboratories, Inc., 2008
201 Broadway, Cambridge, Massachusetts 02139

Outdoor-to-Indoor Office MIMO Measurements and Analysis at 5.2 GHz

Shurjeel Wyne, *Student Member, IEEE*, Andreas F. Molisch, *Fellow, IEEE*, Peter Almers, Gunnar Eriksson, Johan Karedal, *Student Member, IEEE*, and Fredrik Tufvesson, *Senior Member, IEEE*

***Abstract*—The outdoor-to-indoor wireless propagation channel is of interest for cellular and wireless local area network applications. This paper presents the measurement results and analysis based on our multiple-input–multiple-output (MIMO) measurement campaign, which is one of the first to characterize the outdoor-to-indoor channel. The measurements were performed at 5.2 GHz; the receiver was placed indoors at 53 different locations in an office building, and the transmitter was placed at three "base station" positions on a nearby rooftop. We report on the root-mean-square (RMS) angular spread, building penetration, and other statistical parameters that characterize the channel. Our analysis is focused on three MIMO channel assumptions often used in stochastic models. 1) It is commonly assumed that the channel matrix can be represented as a sum of a line-of-sight (LOS) contribution and a zero-mean complex Gaussian distribution. Our investigation shows that this model does *not* adequately represent our measurement data. 2) It is often assumed that the Rician K-factor is equal to the power ratio of the LOS component and the other multipath components (MPCs). We show that this is not the case, and we highlight the difference between the Rician K-factor often associated with LOS channels and a similar power ratio for the estimated LOS MPC. 3) A widespread assumption is that the full correlation matrix of the channel can be decomposed into a Kronecker product of the correlation matrices at the transmit and receive array. Our investigations show that the direction-of-arrival (DOA) spectrum noticeably depends on the direction-of-departure (DOD); therefore, the Kronecker model is not applicable, and models with less-restrictive assumptions on the channel, e.g., the Weichselberger model or the full correlation model, should be used.**

***Index Terms*—Angular dispersion, channel sounding, direction-of-arrival (DOA), direction-of-departure (DOD), Kronecker model, line-of-sight (LOS) power factor, multiple-input multiple-output (MIMO), Rician K-factor, virtual channel representation (VCR), Weichselberger model.**

I. Introduction

MULTIPLE-INPUT–multiple-output (MIMO) systems can result in tremendous capacity improvements over single-antenna systems [1], [2]. However, the capacity gains depend on the propagation channel in which the system operates. The most important requirement for any channel model is agreement with reality; hence, the measurement of propagation channels and the subsequent parameterization of models based on these measurements are critically important. There have been a number of double-directional outdoor-to-outdoor and indoor-to-indoor measurement results reported in the literature, e.g., [3]–[7]. However, there has been a remarkable lack of outdoor-to-indoor measurement results, although the outdoor-to-indoor scenario has important applications for voice–data transmission in third-generation cellular systems as well as wireless local area networks. The measurement campaign reported in this paper (first published in [8]), together with [9] and [10], is the first published result of outdoor-to-indoor measurements characterizing the MIMO channel.

There are two main categories of channel models for MIMO systems, both of which will be used in this paper. The *double-directional* channel models [3] describe the MIMO channel by parameters of the multipath components (MPCs): direction-of-departure (DOD), direction-of-arrival (DOA), delay, and complex amplitudes. A double-directional channel characterization is highly useful because it is independent of antenna configurations, describes the physical propagation alone, and serves to point out the dominant propagation mechanisms. On the other hand, *analytical* channel models describe the statistics of the transfer function matrix. Each entry in that matrix gives the transfer function from the ith transmit to the jth receive antenna element. Almost all of the analytical channel models, with the exception of the keyhole model [11], are based on the assumption that the entries of the transfer function matrix are *zero-mean* complex Gaussian, with the possible addition of a line-of-sight (LOS) component. Furthermore, many models describe the correlation matrix of those entries as a Kronecker product of the correlation matrices at the transmit and receive sides. The first assumption has, to our knowledge, generally remained unquestioned.[1] The Kronecker assumption has been

Manuscript received August 27, 2006; revised May 28, 2007 and July 22, 2007. This work was supported in part by the Swedish Foundation for Strategic Research under an INGVAR Grant, in part by the Swedish Science Council, and in part by the SSF Inter-University Center of Excellence for High-Speed Wireless Communications. This paper was presented in part at the IEEE Vehicular Technology Conference (VTC), Los Angeles, CA, September 2004 (Fall), and IEEE VTC 2005 Spring. The review of this paper was coordinated by Dr. K. Dandekar.

S. Wyne, P. Almers, J. Karedal, and F. Tufvesson are with the Department of Electrical and Information Technology, Lund University, 221 00 Lund, Sweden (e-mail: Shurjeel.Wyne@eit.lth.se; Peter.Almers@eit.lth.se; Johan.Karedal@eit.lth.se; Fredrik.Tufvesson@eit.lth.se).

A. F. Molisch is with Mitsubishi Electric Research Labs, Cambridge, MA 02139, USA, and also with the Department of Electrical and Information Technology, Lund University, 221 00 Lund, Sweden (e-mail:Andreas.Molisch@ieee.org).

G. Eriksson is with the Department of Electrical and Information Technology, Lund University, 221 00 Lund, Sweden, and also with the Swedish Defence Research Agency, 581 11 Linköping, Sweden (e-mail: guneri@foi.se).

Color versions of one or more of the figures in this paper are available online at http://ieeexplore.ieee.org.

Digital Object Identifier 10.1109/TVT.2007.909272

[1] With the exception of the rare "keyhole scenario" (see [11] and [12]).

0018-9545/$25.00 © 2008 IEEE

recently more extensively discussed [7], [13]. Considering that the measurement data from outdoor scenarios seem to indicate good agreement with this assumption [13], the indoor data seem to deviate more [14], and, as a consequence, a more general model has, e.g., been developed by Weichselberger *et al.* [7].

In this paper, we present the results of a double-directional MIMO channel measurement campaign for an outdoor-to-indoor office scenario (carried out at 5.2 GHz) and evaluate the validity of the standard assumptions of analytical channel models (the first results were published in [15]). Our main contributions are the following.

- We analyze the DOD and DOA and discuss the dominant propagation mechanisms.
- We give the distributions of root-mean-square (RMS) directional spreads and delay spreads.
- We present a statistical analysis of the measured fading and compare it with popular models.
- We investigate the validity of the "LOS-plus-Gaussian-remainder" assumption and show that it does not hold for all measurement locations in our campaign.
- We explain this result by investigating in detail the difference between "LOS power factor" and "Rician K-factor."
- We analyze the validity of the Kronecker model and present detailed results on the coupling between DOAs and DODs.

This paper is organized as follows. Section II describes the measurement setup and scenario and the procedure for data evaluation. In Section III, the physical propagation processes are described. Furthermore, Section IV contains an analysis of the dispersion in angular and delay domains, and Section V compares three analytical channel models. Finally, in Section VI, we summarize the results.

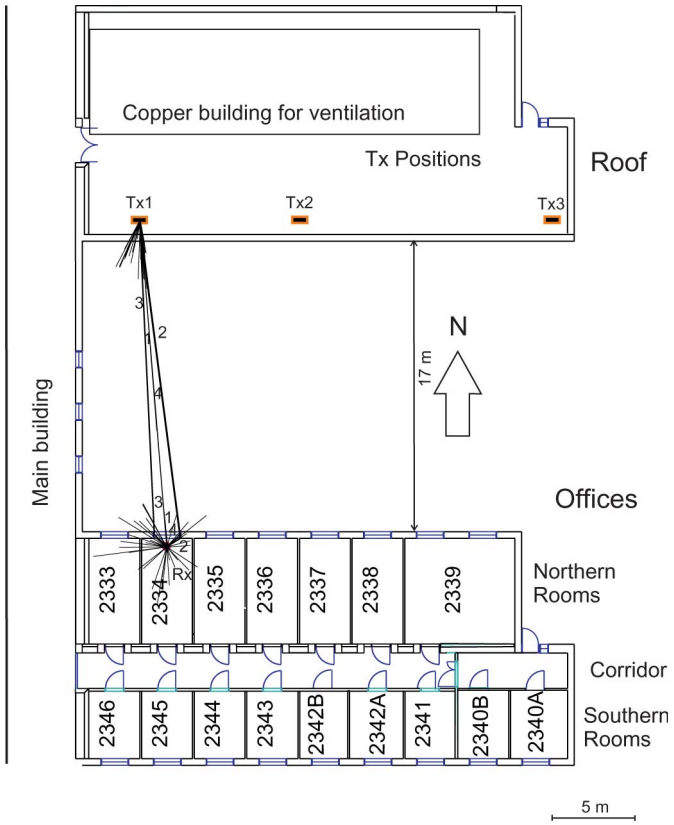

Fig. 1. Site map showing the locations of Tx (second floor) and Rx positions (first floor). The free space distance between the blocks is also indicated. The 4–7 positions were measured in rooms 2334, 2336, 2337, and 2339 (referred to as north) and 2345, 2343, 2342A, and 2340B (referred to as south).

II. Measurement Setup and Evaluation

A. Equipment and Scenario

For the measurements, we used the RUSK ATM [16] channel sounder to measure the transfer function between transmit (Tx) and receive (Rx) antenna elements. This sounder uses the multiplexing principle (subsequently connecting the Tx, and Rx, antenna elements to the radio frequency chains) for obtaining MIMO transfer function matrices. The measurements were performed at a center frequency of 5.2 GHz and a signal bandwidth of 120 MHz using a transmit power of 33 dBm. The Tx antenna was an eight-element dual-polarized uniform linear array (ULA) of patch elements with element spacing $\approx \lambda/2$ (half wavelength). We only considered the eight vertically polarized elements in our analysis. The Rx antenna was a 16-element uniform circular array (UCA) of vertically polarized monopole elements (radius $\approx \lambda$). Both array configurations were calibrated prior to measurement so that the array response data were available for the application of high-resolution algorithms. The Tx signal had a period of 1.6 μs, and the sampling time for one MIMO snapshot was 819 μs, which is within the coherence time of the channel. At each Rx location, 13 snapshots were measured with a time spacing of 4.1 ms between successive snapshots. Our measurement results directly give the channel transfer function matrix sampled at 193 frequency subchannels. For the double-directional channel characterization, we needed the parameters like delay, DOA, DOD, and complex amplitude of the MPCs. Those were obtained with the high-resolution SAGE algorithm [17] (see Section II-B for details).

The test site is the E building at Lund University, Lund, Sweden. A map of the site is shown in Fig. 1. The transmitter was placed at three different positions on the roof of a nearby building. For each Tx position, the receiver was placed at 53 measurement positions located in eight different rooms and the corridor between the rooms. The measurement positions in each room were placed on a 3×3 grid spanning an area of approximately 6×3 m^2. The three positions in the north–south direction were denoted north, middle, and south, and the three positions in the east–west direction were denoted east, middle, and west. The Rx position in a room was described by a pair of letters suffixed to the room number to indicate the north–south and east–west positions, respectively. As a sample result, Fig. 1 shows the strongest four of the estimated MPCs for Tx position 1 and receiver placed at 2334 NM.

B. SAGE Analysis

1) Signal Model: The data evaluation is based on the assumption that the received and transmitted signals can be

described as a finite number of plane waves [18], i.e.,

$$h_{m,n}\left(k,i,\alpha_l,\tau_l,\phi_l^{\mathrm{Rx}},\phi_l^{\mathrm{Tx}},\nu_l\right) = \sum_{l=1}^{L}\alpha_l e^{-j2\pi\Delta f\tau_l k}G_{\mathrm{Tx}}\left(n,\phi_l^{\mathrm{Tx}}\right)G_{\mathrm{Rx}}\left(m,\phi_l^{\mathrm{Rx}}\right)e^{j2\pi\Delta t\nu_l i} \quad (1)$$

where L is the total number of extracted MPCs, and α_l, τ_l, ϕ_l^{Rx}, ϕ_l^{Tx}, and ν_l are the complex amplitude, delay, DOA in azimuth, DOD in azimuth, and Doppler frequency, respectively, of the lth MPC. The impact of elevation is neglected. Furthermore, k, i, m, n, G_{Rx}, and G_{Tx} are the frequency subchannel index, snapshot index, Rx element number, Tx element number, Rx antenna pattern, and Tx antenna pattern, respectively. Based on this data model, the SAGE algorithm can, using an iterative method, provide a maximum-likelihood estimate of the MPC parameters from the measured transfer functions. In our evaluations, we used 30 iterations of the algorithm.

All 13 snapshots that were taken at a given Rx position were used in data processing, with 40 MPCs being extracted from each measurement position. The path parameters, DOA, DOD, and delay were cross checked at a number of positions with the geometry of the measurement site and provided a good match. It must be stressed that the high-resolution algorithms based on the sum-of-plane-waves model cannot explain all the possible propagation processes. For example, diffuse reflections and spherical waves are not covered by the model of (1). For this reason, the total power of the MPCs extracted by SAGE does not necessarily equal the total power of the signals observed at the antenna elements. This can be compounded by the fact that for some locations, more than 40 MPCs might carry significant energy. A quantitative discussion of this is given in Section II-B2.

The estimated Doppler frequency for most MPCs was less than 1 Hz, although at a few locations, Doppler frequencies of around 2–3 Hz were measured. Since the inverse of the Doppler frequency was significantly larger than the total measurement duration of 13 snapshots, this indicates a relatively static measurement scenario.

2) Relative Extracted Power: The received power estimated by SAGE is dependent on, e.g., the environment and the number of extracted MPCs L. The relative extracted power is computed as[2]

$$Q(L) = \frac{\left\|\hat{\mathbf{H}}(L)\right\|_F^2}{\|\mathbf{H}_{\mathrm{meas}}\|_F^2 - \hat{\sigma}_n^2} \quad (2)$$

where $\mathbf{H}_{\mathrm{meas}}$ is the measured transfer matrix, and $\hat{\mathbf{H}}(L)$ is the channel matrix reconstructed from the SAGE estimates of $L = 40$ MPCs inserted into the channel model of (1). The estimate of the noise power $\hat{\sigma}_n^2$ was calculated at each measurement position as

$$\hat{\sigma}_n^2 = \sum_{i=1}^{I-1}\frac{\|\mathbf{H}_{i+1} - \mathbf{H}_i\|_F^2}{2(I-1)} \quad (3)$$

where $\mathbf{H}_i$ is the measured channel transfer matrix for the ith snapshot, and I is the total number of snapshots. This noise estimation was possible because we have an (approximately) time-invariant channel, which we confirmed from our measurements (see above). The cumulative distribution function (CDF) of the relative extracted power is shown for all 159 locations in Fig. 2. As shown in the figure, the extracted power with a source order of 40 significantly varies over the measurement locations. In the majority of measurement locations, more than 85% of the power is captured, although at some positions, only about 60% of the power is captured.

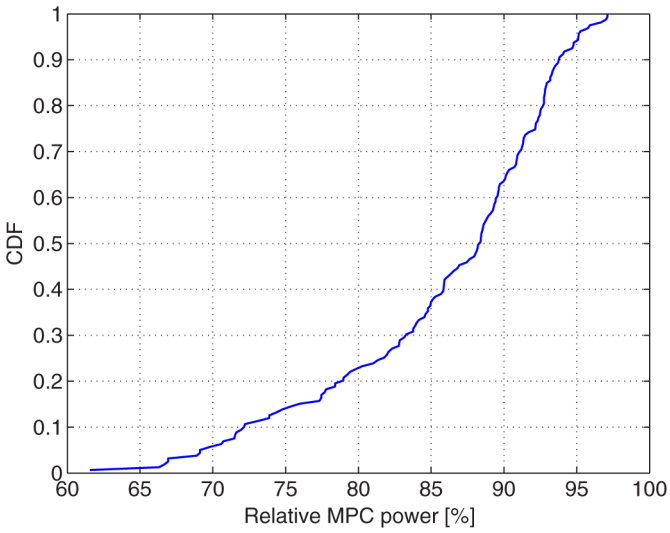

Fig. 2. CDF of the power captured by 40 estimated MPCs, expressed as the percentage of the power calculated from the measured transfer matrix. All 159 measurement positions have been used in calculating the CDF.

3) Source Order Effects: For different initial estimates of the source order, we have investigated the mean square reconstruction error between the measured data and the matrix reconstructed from MPC parameters estimated by SAGE. For each initial estimate of the source order in the range from 1 to 100 MPCs, the mean square relative reconstruction error (MSRRE) was defined as

$$\mathrm{MSRRE} = E\left[\frac{\|\mathbf{H}_{\mathrm{meas}} - \hat{\mathbf{H}}_{\mathrm{reconstruct}}\|_F^2}{\|\mathbf{H}_{\mathrm{meas}}\|_F^2}\right] \quad (4)$$

where $\mathbf{H}_{\mathrm{meas}}$ is the $N_R \times N_T$ measured channel, and $\hat{\mathbf{H}}_{\mathrm{reconstruct}}$ is the matrix reconstructed by (1) from MPCs estimated by SAGE. The expectation is over different frequency subchannels in one measured time snapshot that we use as realizations of the channel. The error from (4) is plotted in Fig. 3 for a typical LOS and non-LOS (NLOS) scenario. It can be observed from Fig. 3 that as we increase the source order (collect more MPCs), the slope of the reconstruction

[2]We use the following notation throughout the paper: $\hat{\mathbf{A}}$ denotes the estimate of $\mathbf{A}$, $\|\mathbf{A}\|_F$ denotes the Frobenius norm of the matrix $\mathbf{A}$, $\mathbf{A}^T$ denotes the transpose $(\mathbf{A})$, $\mathbf{A}^*$ denotes the conjugate $(\mathbf{A})$, $\mathbf{A}^H$ denotes $(\mathbf{A}^*)^T$, and $\mathbf{A}^{1/2}$ is the matrix square root defined in this paper as $\mathbf{A}^{1/2}(\mathbf{A}^{1/2})^H = \mathbf{A}$. The operator vec$\{\mathbf{A}\}$ stacks the columns of $\mathbf{A}$ on top of each other, and un-vec$\{\mathbf{A}\}$ is the inverse operation. Furthermore, $tr\{\mathbf{A}\}$ is trace$(\mathbf{A})$, $\mathbf{A}_{ij}$ is the entry in the ith row and jth column of $\mathbf{A}$, and $\mathbf{A} \odot \mathbf{B}$ is the element-wise product of $\mathbf{A}$ with matrix $\mathbf{B}$. Finally, $\mathbf{G}$ is a random matrix with elements that are independent identically distributed zero-mean circularly symmetric complex Gaussian random variables with unit variance.

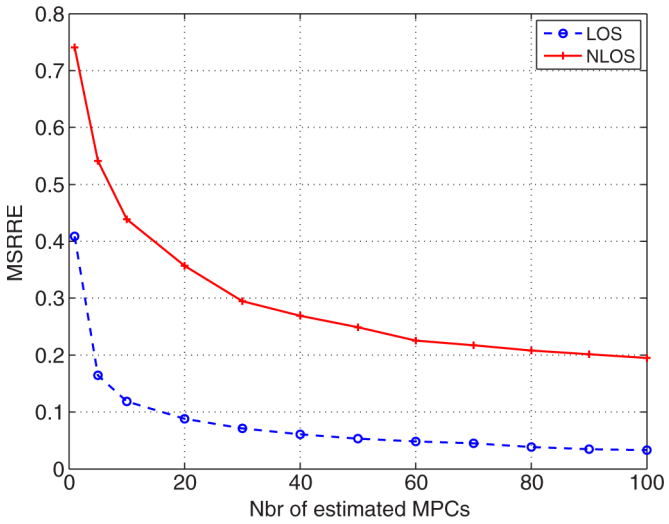

Fig. 3. MSRRE between measured data and the SAGE signal model for different source orders. A typical LOS and NLOS scenario is shown.

error flattens out, which can be interpreted as an indication that we begin to estimate noise spikes (or that we begin to estimate wave parameters that have small correlation peaks in the M-step of the SAGE). By extracting 40 MPCs at each location, we are not in the flat part of the reconstruction error curve, which suggests that we do not estimate noise spikes as specular components. As a further check, we have also verified for each measurement that the difference in power between the strongest and weakest MPCs estimated by SAGE is within the dynamic range of our channel sounder and within the sum (in decibels) of the correlation gain provided by SAGE and the measurement SNR at the respective location to lower the probability that we estimate noise spikes. Although Fig. 3 may suggest that extracting 40 MPCs could lead to an underestimated source order, particularly for the NLOS scenarios, we believe (based on sample evaluations not presented here) that the potential difference in source order will not significantly alter the results presented in this paper. In general, a correct source order estimation is an open research topic, and, in the extreme case, a source order of a few thousand has been used [19].

III. Physical Propagation Processes

In Fig. 4, the 40 extracted MPCs are plotted for each of the 53 Rx positions corresponding to Tx position 1. The line lengths represent the MPC amplitudes at each measurement location, relative to the strongest MPC at the same location.

This figure allows us to make some important conclusions about the dominant propagation processes.

1) In the north rooms, propagation through walls and windows shows an almost equal efficiency, as one can see from the (relative) strength of the LOS components in the different rooms. The reason lies in the strong attenuation by the windows and walls. The (exterior) walls consist of bricks and reinforced concrete, whereas the windows are coated with a metallic film for energy conservation.[3] Additional measurements of the propagation characteristics of walls and windows showed that the attenuation of the windows is actually slightly larger than the attenuation of the walls.
2) The reflection and diffraction by the window frames are efficient propagation mechanisms. This is evident, e.g., from the DOAs in rooms 2334 and 2336. It is particularly noteworthy that the propagation via the frames of the windows results in an attenuation similar to the attenuation of the brick wall, e.g., see the delay–azimuth plots for position Tx1Rx2336NM in Fig. 5.
3) Each window is split into two glass panes by a horizontal middle section with a metal handle and locking mechanism. There are strong MPCs coming from the window direction; see, e.g., position Tx1Rx2336NM. The delay–azimuth plot in Fig. 5 shows a number of MPCs of similar strength and very similar delays (note that the DOAs are around 180°, which corresponds to the window direction).
4) For some south rooms, propagation through north rooms via doors constitutes a strong propagation mechanism. This is clearly shown, e.g., in the delay–azimuth plot for position Tx1Rx2343SM in Fig. 5.
5) There are strong reflections observed in the south rooms coming from the south. These reflections are from structures along the south walls of the rooms, e.g., metal pipes of heaters mounted on the south wall (refer to Fig. 5 for position Tx1Rx2343SM).
6) While the strengths of the MPCs are widely differing, the directions of the MPCs are more uniformly distributed. Typically, only two or three MPCs show similar DOAs, e.g., refer to Fig. 4. On the other hand, all the DODs are closely grouped together.

Similar results were observed for all three Tx positions.

IV. Statistical Analysis of Angular and Delay Dispersion

A. Angular Dispersion

The angular dispersion is an important parameter for the characterization of a spatial channel. In this paper, we use *direction spread* [20] as a measure for the angular dispersion. The *direction spread* parameter does not suffer from the ambiguity related to the choice of the origin of the coordinate system. The RMS direction spread is calculated as[4]

$$\sigma_{\text{ang}} = \sqrt{\sum_{l=1}^{L} |e^{j\phi_l} - \mu_{\text{ang}}|^2 P_{\text{ang}}(\phi_l)} \tag{5}$$

where

$$\mu_{\text{ang}} = \sum_{l=1}^{L} e^{j\phi_l} P_{\text{ang}}(\phi_l). \tag{6}$$

[3]In most countries with a cold climate, such metal-coated windows are typically used in residential and office buildings.

[4]In [20], "direction" is given by the unity vector in the spherical coordinate system. The *direction spread* is a dimensionless quantity.

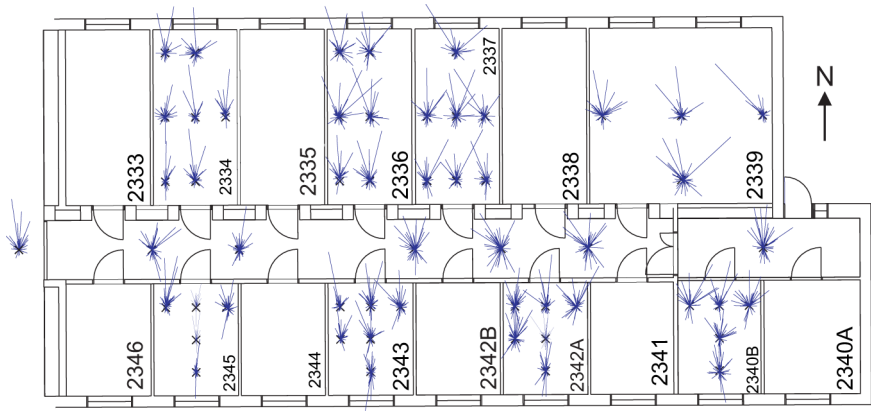

Fig. 4. DOAs at all the receiver positions for transmit position 1. North corresponds to 180° DOA.

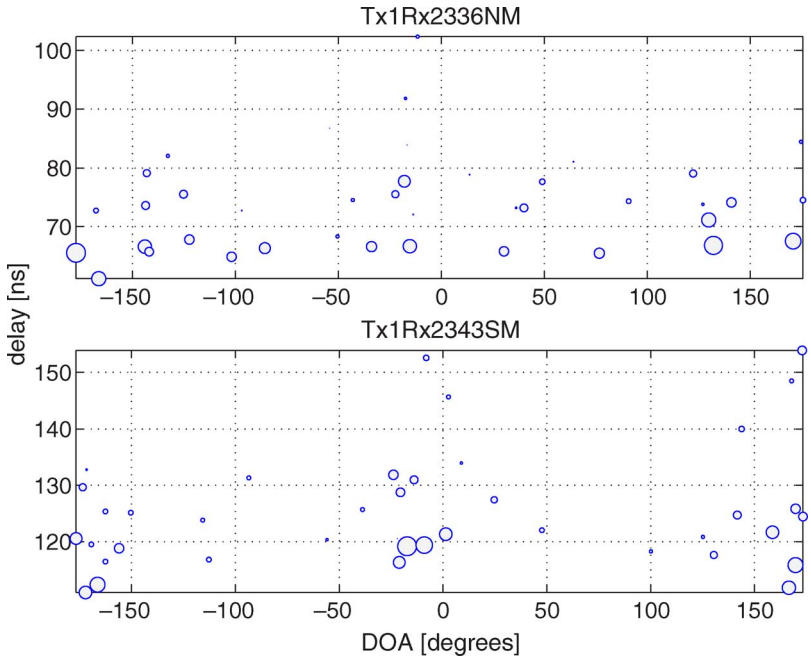

Fig. 5. Joint delay–azimuth plot for two Rx positions. The marker diameter is scaled according to the relative power (in decibels) of each MPC, and the MPC powers are normalized with the power of the strongest MPC extracted at the respective Rx position. The measurement position is indicated in each subplot. Note the different scaling for the delay axis.

$P_{\mathrm{ang}}(\phi_l)$ is the angular power spectrum normalized as $\sum_L P_{\mathrm{ang}}(\phi_l) = 1$. Figs. 6 and 7 present the CDF of the DOA and DOD spreads for different Tx and Rx locations. The differences between the north and south rooms are evident, particularly at the Rx side. In the corridor, the spread is close to that of the south offices.

The mean direction spreads are presented in Table I. We can immediately see that the angular dispersion at the Rx is markedly higher than for the Tx. This result is intuitive, as the Tx is located outdoors and radiates only toward the Rx, whereas the Rx sees MPCs that can come through the windows and walls or are reflected from walls all around the Rx. Furthermore, it is evident that the transmit position does not affect the mean value of the DOA spread, and there is no large difference in mean spread for the north rooms, corridor, and the south rooms. However, there are large differences in the DOD spread for the different transmit positions. The coupling between the DOAs and DODs will be discussed in Section V-C.

B. Delay Dispersion

The RMS delay spread roughly characterizes the multipath propagation in the delay domain and is conventionally defined as [21]

$$\sigma_\tau = \sqrt{\bar{\tau^2} - (\bar{\tau})^2} \tag{7}$$

where the mean excess delay $\bar{\tau}$ and the noncentral second moment of the average power delay profile $\bar{\tau^2}$ are defined as [21]

$$\bar{\tau} = \frac{\sum_L P_{\mathrm{del}}(\tau_l)\tau_l}{\sum_L P_{\mathrm{del}}(\tau_l)} \quad \text{and} \quad \bar{\tau^2} = \frac{\sum_L P_{\mathrm{del}}(\tau_l)\tau_l^2}{\sum_L P_{\mathrm{del}}(\tau_l)} \tag{8}$$

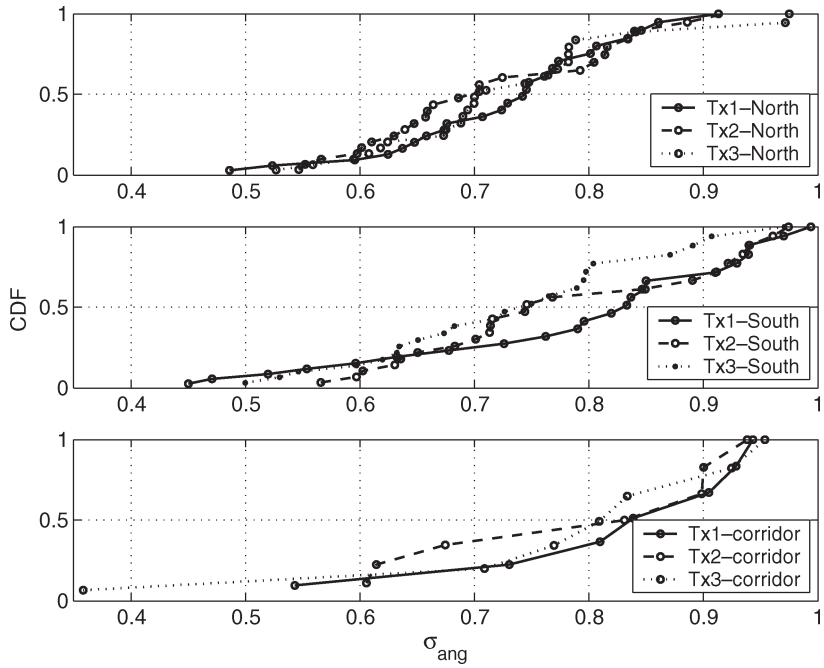

Fig. 6. CDFs of the RMS DOA spread. The subplots from top to bottom are for the north rooms, south rooms, and the corridor, respectively.

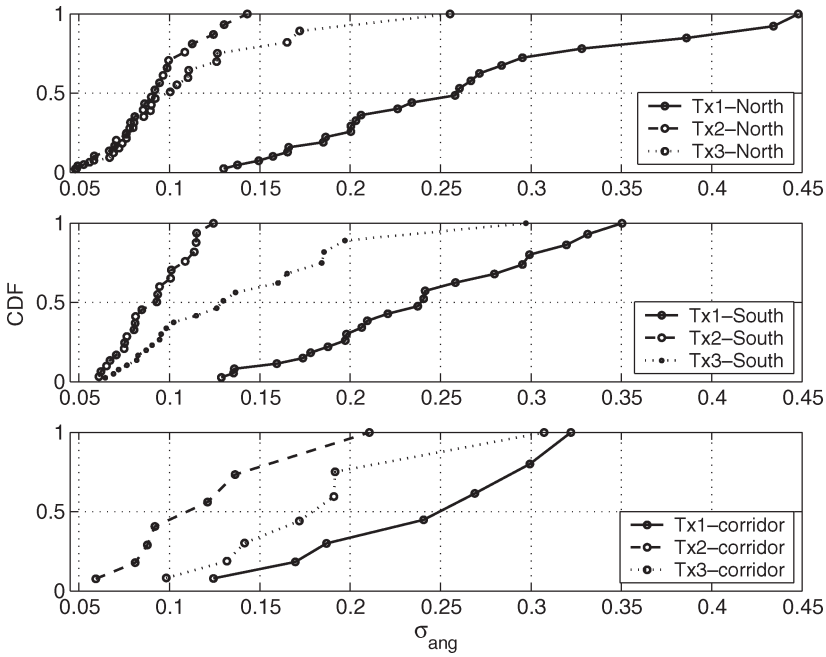

Fig. 7. CDFs of the RMS DOD spread. The subplots from top to bottom are for the north rooms, south rooms, and the corridor, respectively.

where $P_{\mathrm{del}}(\tau_l)$ is the delay power spectrum, and τ_l is the delay of the lth MPC. Fig. 8 presents the CDF for the RMS delay spread in the north and south rooms. The delay spread has been evaluated using the MPCs as extracted from the SAGE algorithm. This has the drawback that diffuse contributions are not reflected in the obtained delay spreads (which, therefore, tend to be somewhat low). On the other hand, delay spread values that are directly extracted from the measured power delay profiles show too many high values, as noise contributions at large delays have a disproportionate influence. The usual technique of thresholding the average power delay profile (for noise reduction) cannot be applied in our case, since, in some cases, the measurement SNRs are too low for this purpose.[5]

[5]Note that the low SNR problem is mitigated when evaluating the delay spread based on the MPCs. The SAGE algorithm estimates the MPC parameters, including delays by maximizing a correlation function. Due to a large correlation gain accumulated over a typical number of space, time, and frequency samples employed in measurements, the wave parameters can be reliably estimated from a noisy environment. The correlation gain from our measurement parameters (16×8 MIMO, 193 frequency subchannels, and 13 time snapshots) is in excess of 50 dB.

TABLE I
MEAN DIRECTION SPREAD

DOA	$\bar{\sigma}_{\text{ang}}$		
	north rooms	corridor	south rooms
Tx1	0.69	0.82	0.75
Tx2	0.69	0.75	0.75
Tx3	0.69	0.75	0.69
DOD	$\bar{\sigma}_{\text{ang}}$		
	north rooms	corridor	south rooms
Tx1	0.24	0.24	0.23
Tx2	0.09	0.11	0.09
Tx3	0.10	0.18	0.13

Therefore, the delay spread values obtained from the MPC parameters were deemed more reliable.

For the measured outdoor-to-indoor scenario, a cluster analysis of the MPCs has also been performed in the delay–DOA–DOD parameter space. The results are reported in [22].

V. STATISTICAL ANALYSIS

A. LOS Scenario—Fading Statistics

It is widely assumed that in LOS scenarios, the channel coefficients have a *nonzero*-mean complex Gaussian distribution; this results in a Rician distribution of the amplitudes. The measured channel matrix can be modeled as the weighted sum of an estimated LOS contribution (deterministic) and a residue component drawn from a *zero-mean* complex Gaussian distribution [23], i.e.,

$$\mathbf{H}_{\text{model}}(m) = \sqrt{\kappa}\mathbf{H}_{\text{LOS}}^{(n)} + \sqrt{1-\kappa}\mathbf{H}_{\text{res}}^{(n)}(m) \tag{9}$$

$$= \sqrt{\kappa}\mathbf{H}_{\text{LOS}}^{(n)} + \sqrt{1-\kappa}\cdot \text{ un-vec}\{\mathbf{R}^{1/2}\mathbf{G}\} \tag{10}$$

where $\mathbf{H}_{\text{LOS}}$ is the LOS contribution, $\mathbf{H}_{\text{res}}(m)$ is the residue in the mth realization of the channel model, and the superscript (n) represents the fact that the matrices are normalized as $E[\|\mathbf{H}\|_F^2] = N_R N_T$. The scalar $\kappa = (K_{\text{LOS}}/(K_{\text{LOS}}+1))$, where K_{LOS} is the LOS power factor defined as $K_{\text{LOS}} =$ (power in LOS component/power in all other components) (see Section V-B). The full channel correlation matrix $\mathbf{R}$ is estimated as

$$\hat{\mathbf{R}} = \frac{1}{M}\sum_{\mathbf{m}=1}^{\mathbf{M}} \text{vec}\left\{\hat{\mathbf{H}}_{\text{res}}^{(n)}(m)\right\} \text{vec}\left\{\hat{\mathbf{H}}_{\text{res}}^{(n)}(m)\right\}^H. \tag{11}$$

In this paper, a measured scenario is treated as an LOS scenario if the strongest estimated MPC has a DOA and DOD that correspond to the hypothetical line connecting the Tx antenna to the Rx antenna. Note that due to this definition of the LOS, a specific antenna element need not have an LOS, although the array is defined to be in an LOS scenario. We have analyzed the validity of the modeling approach in (9) for our LOS scenarios and found that it is not well fulfilled for all our measured data. For example, the data in Fig. 9 have been taken from an LOS scenario; the top figure shows that the magnitudes of the measured channel coefficients do not exhibit a Rician distribution, although after subtracting the estimated LOS contribution, the residue component has a Rayleigh distribution. The CDF is based on the data from a single measurement location, such that both spatial realizations and the 193 frequency subchannels constitute the statistical ensemble. In an attempt to fit various theoretical distributions to the amplitude of the LOS data, we found that the *generalized Gamma* distribution [24], [25] best represented our measurements. The CDF of the distribution can be expressed as the *incomplete Gamma* function [26]

$$\text{Prob}_{GG}(r < r_0) = P\left(\alpha, \left(\frac{r_0}{\beta}\right)^c\right) \tag{12}$$

where $P(\cdot)$ is the incomplete Gamma function, and α, β, and c are the distribution parameters with $\beta = \sqrt{E[r^2]((\Gamma(\alpha))/(\Gamma(c\alpha+2/c)))}$, and $\Gamma(\cdot)$ is the Gamma function [27]. For all the LOS scenarios that were analyzed, the theoretical CDF of (12) provided a good fit to the measured data with α in the range 1.2–3.5 and c in the range 0.7–1.6. For the residue channel as well as NLOS scenarios, the parameter values $c = 2$ and $\alpha = 1$, which correspond to a Rayleigh fading statistic [25], provide a good match to the measured data distribution.

The generalized Gamma distribution has been used in [28] to represent a composite fading distribution. We investigated possible reasons why the fading distribution in our LOS scenarios deviated from the "standard" model and found that some Rx elements experienced shadow fading, i.e., the mean received power at the Rx elements considerably varied over the array. The shadow fading was a consequence of the absorber[6] that was part of the array construction; see Fig. 10(a).

Fig. 10(b), together with Fig. 11, illustrates how the absorber attenuates the LOS contribution received at the back elements of the array. Therefore, the fading distribution of the channel coefficients becomes a function of which Rx elements are considered for the ensemble. We conjecture that a similar effect would be found with a circular array of patch antennas. Thus, as an important consequence of our investigation, we find that the "standard" model of (9) is applicable for some specific receiver configurations, and the definition of, e.g., a Rice factor based on the model is meaningful. However, the model is not universally applicable, i.e., in LOS scenarios, the small-scale fading statistics may not necessarily be Rician. In our case, it is shadowing due to the array configuration that causes a composite fading distribution over a small-scale area, the Rx array, and the generalized Gamma distribution rather than the Rician is in good agreement with the measured LOS data.

B. LOS Power Factor and Rician K-Factor

We make a distinction between the conventional Rician K-factor K_{Rice} and what we term the LOS power factor K_{LOS}. We define the latter as

$$K_{\text{LOS}} = \frac{E\left[\|\hat{\mathbf{H}}_{\text{LOS}}\|_F^2\right]}{E\left[\|\hat{\mathbf{H}}_{\text{res}}\|_F^2\right]}. \tag{13}$$

[6]The absorber suppresses the back-lobe of the elements. This indicates a lower probability of locking into false and local minima in the iterative estimation procedure, and, hence, a better performance of the high-resolution algorithm.

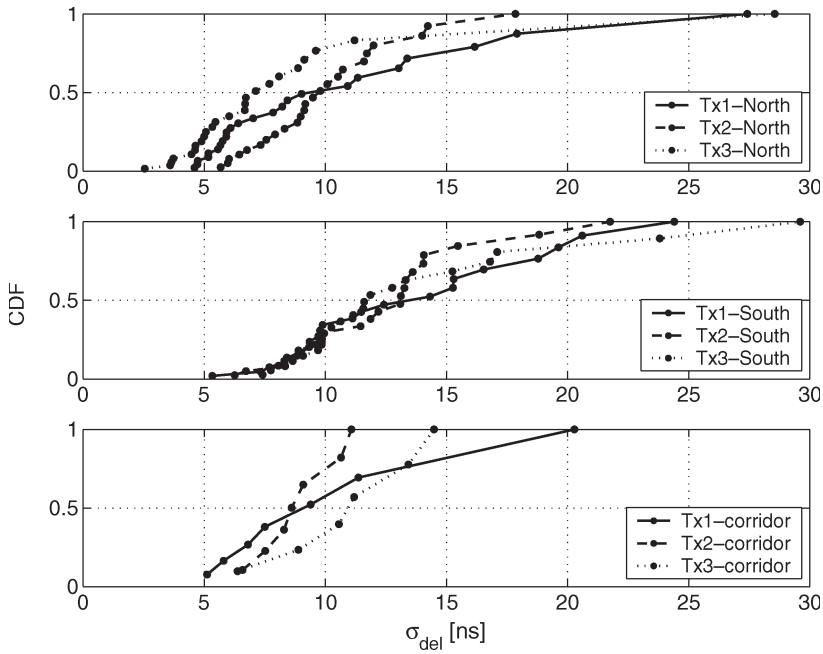

Fig. 8. CDF of the RMS delay spread for the north and south rooms and the corridor.

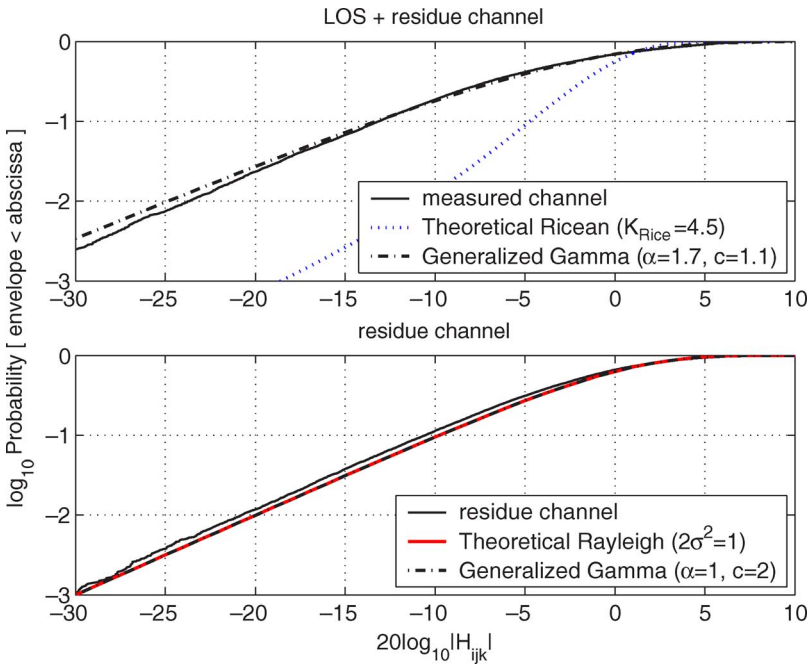

Fig. 9. Generalized Gamma CDF fit to the data distribution for position Tx1Rx2334SM. The top figure shows the measured channel, whereas the bottom figure shows the estimated residue channel. Note that in the bottom figure, the generalized Gamma curve is exactly traced over the Rayleigh curve.

It is essentially the ratio between the power in the estimated LOS component and the power in all the other components. The LOS estimate $\hat{\mathbf{H}}_{\mathrm{LOS}}$ can be extracted from a high-resolution algorithm such as SAGE by inserting channel parameters of the LOS path into the signal model assumed by the algorithm. Note that matrices with unnormalized power are used in calculating K_{LOS}.

It should be stressed that K_{LOS} is different from K_{Rice}. The LOS power factor physically relates to the LOS component, which is strong but is not necessarily the only strong component present in the measured scenario. Still, it can be uniquely identified in a MIMO scenario by its DOA and DOD (they have to agree with the angles that correspond to the "direct line" between the Tx and Rx antennas). On the other hand, K_{Rice} is a characteristic parameter of the Rician amplitude distribution. It is conventionally related to the *narrowband* amplitude distribution; even when it is used to describe the amplitude characteristics of the first delay bin, it does not have a strict correspondence to the LOS component. The Rician K-factors can be extracted, e.g., with the method-of-moments, as suggested by Greenstein *et al.* [29]. Table II compares the estimated values of K_{Rice} and K_{LOS} in some of our measured

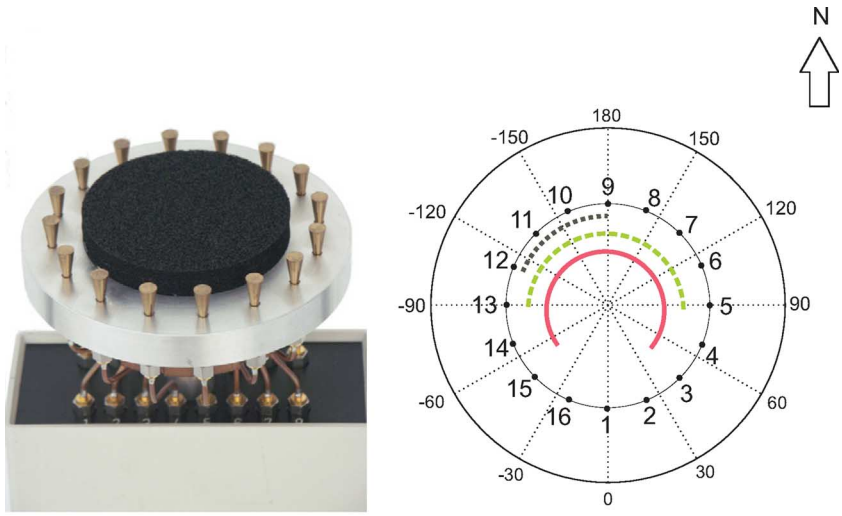

Fig. 10. (a) Rx array is a 16-element vertically polarized UCA; the absorber is shown in the middle. (b) Orientation of UCA elements with respect to angle measure 0° to 180° in either direction of rotation. The element numbers (1–16) are indicated along the circumference of the UCA, and the arcs relate the Rx elements to the corresponding CDFs in Fig. 11.

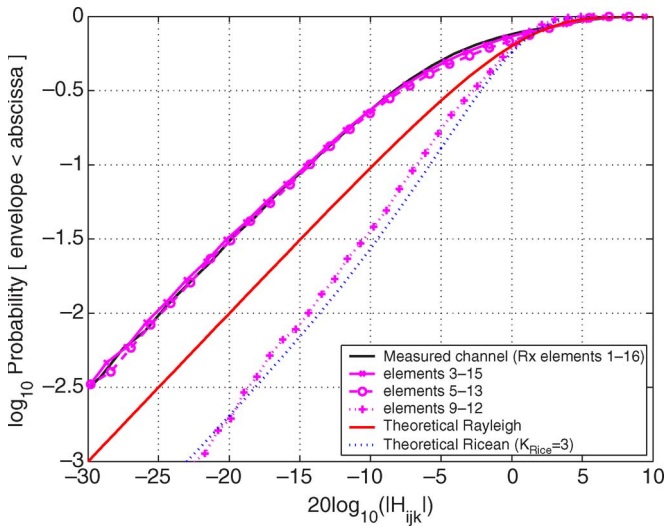

Fig. 11. Measured channel. Effect of selecting Rx elements on the fading distribution of the channel coefficients. Position Tx2Rx2337ME.

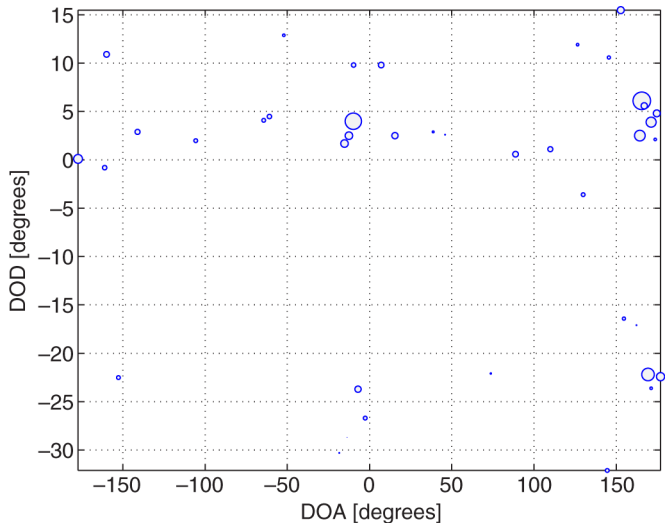

Fig. 12. Joint DOA–DOD plot for Rx position Tx1Rx2345SM. The marker diameter is scaled according to the power of each MPC relative to the power of the strongest component [decibel scale].

TABLE II
COMPARISON OF LOS POWER FACTOR AND RICIAN K-FACTOR IN A RICIAN CHANNEL

Position	Rx elements	K_{LOS}	K_{Rice}
Tx1 Rx2334MM	8-11	2.5	4.3
Tx1 Rx2334SM	8-11	1.6	2.4
Tx1 Rx2337NM	7-10	1.9	2.6
Tx2 Rx2337ME	9-12	2.8	3.0
Tx2 Rx2336NM	7-10	2.2	2.1

locations. A fair comparison between the two parameters requires that the fading distribution in question is Rician, as it would only then be meaningful to talk of a Rician K-factor. To avoid the absorber effect discussed in Section V-A, we selected a subset of four consecutive Rx elements at each measurement location (column 2 in Table II). The selected elements for each measurement position form an arc, which contains the DOA of the respective LOS MPC. The results shown in Table II indicate a general trend that the LOS power factor is different from K_{Rice}. Furthermore, we propose to use K_{LOS} rather than K_{Rice} in modeling LOS scenarios, as in (9). The relative performance of the two metrics in modeling an LOS scenario is discussed further in Section V-C3 (see Fig. 14).

C. Interconnection Between DOAs and DODs

As a third topic of our investigation, we analyze the coupling between the DOAs and DODs. In Fig. 12, the joint DOA–DOD spectrum is shown for one Rx position corresponding to Tx position 1. The plot shows that the joint DOA–DOD spectrum is not separable into the marginal angular spectra. To quantify this effect, we investigate three analytical channel models that make different assumptions about the coupling between DOAs and DODs. All three models share the common

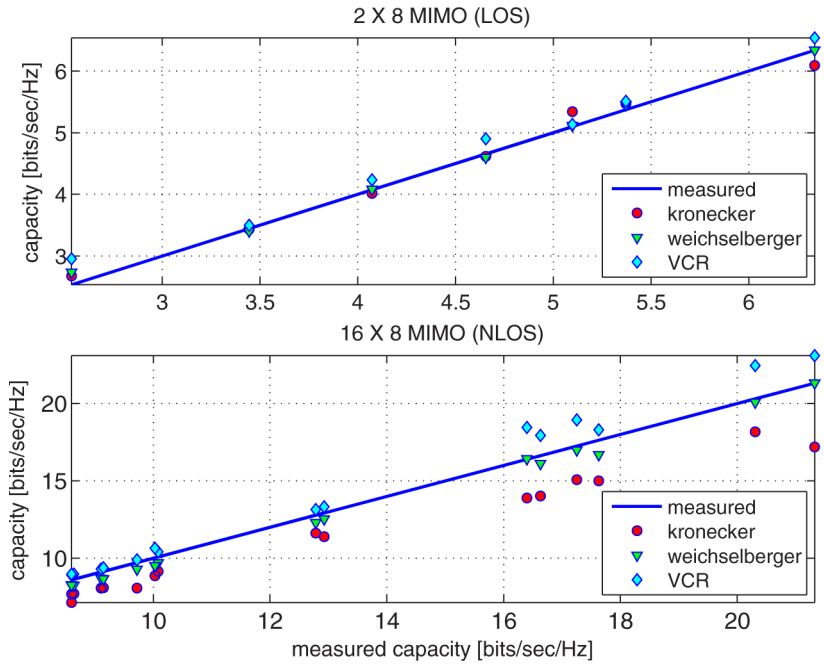

Fig. 13. Scatter plot of average modeled capacity against the average measured capacity of the channel. The top figure is for LOS 2 × 8 MIMO, whereas the bottom figure is for NLOS 16 × 8 MIMO. The identity line indicates points of no modeling error.

assumption that the channel matrix has *zero-mean* complex Gaussian entries. For analyzing the LOS scenarios, we consider only a subset of the full LOS channel matrix, i.e., those rows in the matrix that correspond to Rx elements that receive the LOS component free from the absorber effect. The analysis in Sections V-A and B guarantees that the subset channel has Rician fading. We then model this subset channel according to (9), where only $\mathbf{H}_{\text{res}}$ is modeled by the zero-mean Gaussian models. For NLOS scenarios, no such limitation exists, and we can test the model validity for larger channel matrices.

1) Kronecker Model: The Kronecker model [6], [13] approximates the full channel correlation matrix $\mathbf{R}$ by the Kronecker product of the transmit and receive antenna correlation matrices $\mathbf{R}_{\text{Tx}}$ and $\mathbf{R}_{\text{Rx}}$, respectively. Equivalently, the MIMO channel matrix is modeled as

$$\mathbf{H}_{\text{Kron}} = \frac{1}{\sqrt{tr\{\hat{\mathbf{R}}_{\text{Rx}}\}}} \hat{\mathbf{R}}_{\text{Rx}}^{\frac{1}{2}} \mathbf{G} \hat{\mathbf{R}}_{\text{Tx}}^{\frac{T}{2}}. \tag{14}$$

The Kronecker model assumes that the DOA spectrum, and hence, the structure of the Rx correlation matrix does not change for different DODs.[7] In the context of Fig. 12, the Kronecker assumption, when fulfilled, would imply a rectangular structure, i.e., if one groups the estimated DODs into narrow angular bins, where each bin results in a set of DOAs and path powers according to (1), the Kronecker assumption is considered fulfilled if the DOA power spectrum for each of the DOD bins is similar. We have analyzed the validity of the Kronecker model for both LOS and NLOS scenarios. Fig. 13 shows the modeled ergodic capacity plotted against the measured one for a number of measurement locations. In the top figure (a 2 × 8 LOS setup), the Kronecker model deviates only very little from the measured results. This nice fit is due to the small rank of the channel matrix [30]. The bottom half of Fig. 13 is a 16 × 8 NLOS setup. This setup shows large deviations between the modeled and measured capacity due to the Kronecker assumption about the joint DOA–DOD spectrum. In [7], it is suggested that the Kronecker model, in general, underestimates the channel capacity. This is validated for the outdoor-to-indoor scenario by our results.

Note that the LOS locations considered in Fig. 13 have a measured SNR in the range of 14–20 dB. When computing the ergodic capacity at those locations, the evaluation SNR in the capacity formula was always set to 10 dB below the corresponding measured value. In a previous work [12] that analyzes the impact of measurement noise on capacity, it was established that even for a "keyhole" MIMO channel (in which the capacity is very sensitive to measurement noise), the capacity calculations are correct as long as the measurement SNR is 10 dB better than the evaluation SNR. Thus, our reported results are not influenced by measurement noise. For the NLOS scenarios considered in Fig. 13, the measurement SNR was in a considerably lower range of 1–13 dB. However, we mitigated the measurement noise at each location by coherently averaging the channel matrices over the available 13 time snapshots; this improves the measurement SNR by a factor exceeding 10 dB. For capacity evaluation, we always use the noise-suppressed channel matrices and set the evaluation SNR in the capacity formula to the unprocessed value of the measured SNR so that we have a 10-dB difference between measured and evaluation SNR. Therefore, our NLOS capacity results also represent the true channel capacity.

2) VCR: The virtual channel representation (VCR) was introduced in [31] for a ULA at each link end and allows an arbitrary coupling between predetermined directions at the Tx and

[7]However, the total power in the spectrum, which is a scale factor for the correlation matrix, is allowed to change.

Rx sides. The model uses discrete Fourier transform matrices $\mathbf{A}_{\mathrm{Rx}}$ and $\mathbf{A}_{\mathrm{Tx}}$ at respective link ends such that the measured channel and the virtual channel are unitarily equivalent. The realizations of the channel model can be generated as

$$\mathbf{H}_{\mathrm{VCR}} = \mathbf{A}_{\mathrm{Rx}}(\tilde{\Omega} \odot \mathbf{G})\mathbf{A}_{\mathrm{Tx}}^{T} \tag{15}$$

where the columns of $\mathbf{A}_{\mathrm{Rx}}$ and $\mathbf{A}_{\mathrm{Tx}}$ are based on the array response (steering) vectors computed at fixed virtual directions, and the matrix $\tilde{\Omega}$ is the element-wise square root of the power coupling matrix Ω. The entry Ω_{ij} gives the average power coupled between the ith receive and jth transmit direction. This beamforming approach thus incorporates the antenna array effects. However, since the directions are predetermined, and scatterers within the spatial resolution of the array will not be resolved, it is possible that the true spatial characteristics of the channel will not be accurately rendered for some scenarios.

In our measurement setup, the Rx array was not a ULA but rather a UCA with an absorber in the center. We thus use a generalization of (15) that combines the standard virtual channel model at the Tx side with a "canonical" representation, based on the channel statistics, at the Rx side, i.e.,

$$\mathbf{H}_{\mathrm{VCR}} = \hat{\mathbf{U}}_{\mathrm{Rx}}(\tilde{\Omega} \odot \mathbf{G})\mathbf{A}_{\mathrm{Tx}}^{T}$$

where $\hat{\mathbf{U}}_{\mathrm{Rx}}$ is an estimate of the receive eigenvector matrix obtained by the eigenvalue decomposition of $\hat{\mathbf{R}}_{\mathrm{Rx}}$. In Fig. 13, the ergodic capacities computed from this model are also shown. For the 16×8 NLOS setup, the capacity from this model tends to slightly overestimate the measured values.

3) Weichselberger Model: Like the Kronecker model, the Weichselberger model [7] represents the measured channel in the eigenvector domain, although, unlike the Kronecker model, it strives to jointly model channel correlations at both link ends. This is achieved by defining a power coupling matrix between the eigenvectors of the two link ends. The Weichselberger model assumes that the eigenvector matrix at the Rx is independent of the spatial Tx weight vector, i.e., DOD, that is considered. However, the corresponding eigenvalues of the spatial correlation matrix at Rx can differ for different DODs. The same argument applies to the reverse link. The physical interpretation of the modeling assumptions can be found in [7], wherein the channel is modeled as

$$\hat{\mathbf{H}}_{\mathrm{weichsel}} = \hat{\mathbf{U}}_{\mathrm{Rx}}(\tilde{\Omega} \odot \mathbf{G})\hat{\mathbf{U}}_{\mathrm{Tx}}^{T} \tag{16}$$

where $\hat{\mathbf{U}}_{\mathrm{Rx}}$ and $\hat{\mathbf{U}}_{\mathrm{Tx}}$ are estimates of the receive and transmit eigenvector matrices obtained by the eigenvalue decomposition of $\hat{\mathbf{R}}_{\mathrm{Rx}}$ and $\hat{\mathbf{R}}_{\mathrm{Tx}}$, respectively. The elements of the power coupling matrix Ω_{ij} now give the average power coupled between the ith receive and jth transmit eigenvector; the matrix is estimated as

$$\hat{\Omega} = \frac{1}{M}\sum_{m=1}^{M}[\mathbf{K} \odot \mathbf{K}^{*}] \tag{17}$$

where $\mathbf{K} = (\hat{\mathbf{U}}_{\mathrm{Rx}}^{H}\mathbf{H}(m)\hat{\mathbf{U}}_{\mathrm{Tx}}^{*})$, and $\mathbf{H}(m)$ is the mth channel realization. It should be noted that the Kronecker model is a special case of the Weichselberger model. In Fig. 13, the ergodic capacity computed from the Weichselberger model is shown for the same measurement locations as for the previous cases. Compared to the Kronecker model, the Weichselberger model provides a better fit to the measured data. This result is expected from Fig. 12, where the joint spectrum is not separable into the marginal spectra. The Weichselberger model fits the measured data better than the VCR case as well. This can be explained because in the former case, the channel statistics determine the unitary matrices at *both* link ends. Our results, which were obtained for the outdoor-to-indoor scenario, are consistent with the observations in [7], which separately considered the pure indoor and outdoor cases. As a follow-up to Section V-B, we use the Weichselberger model and the ergodic capacity as a metric to compare the performance of K_{Rice} and K_{LOS} in modeling an LOS scenario according to (9). The plots are shown in Fig. 14 for a 2×8 LOS setup. Although the restriction to use a small rank LOS channel will result in a convergence of performance of the two metrics, from the figure, the K_{LOS} metric appears to perform better.

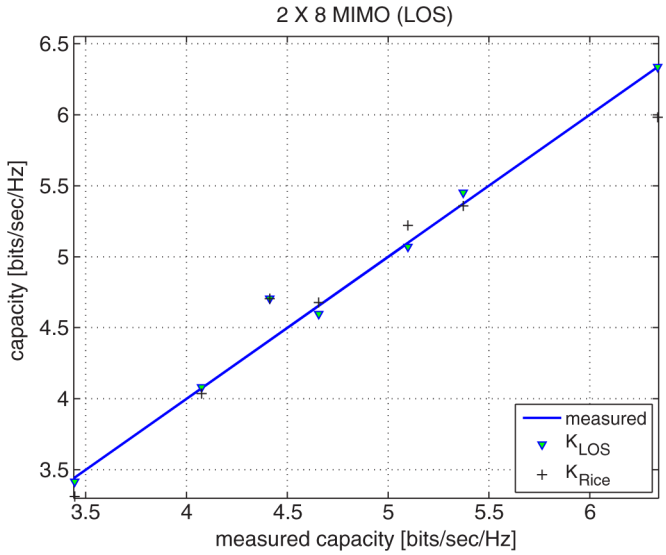

Fig. 14. Performance comparison of K_{LOS} and K_{Rice} in modeling an LOS scenario. The Weichselberger model is used in both cases.

VI. Conclusion

In this paper, we have presented the results of a double-directional measurement campaign for an outdoor-to-indoor office scenario. Our characterization of the outdoor-to-indoor scenario indicates that the angular dispersion at the outdoor link end is rather small; the mean direction spread is in the range of 0.09–0.24. At the indoor link end, MPCs of significant energy arrive from all directions; therefore, the angular dispersion is much larger, we observed mean direction spreads in the range of 0.69–0.82. The delay spread was measured to be in the range of 5–25 ns. By considering 40 MPCs at each measured position, more than 85% of the received power could be accounted for in 60% of the 159 measurement locations.

Our statistical analysis shows that the widely used assumption in MIMO channel modeling, i.e., that the channel can be represented as a sum of a weighted LOS component plus a zero-mean complex Gaussian distribution, may not adequately

represent the measured data. In general, the small-scale fading in an LOS scenario may not be Rician. We observed a composite fading distribution caused by our antenna configuration and found the generalized Gamma distribution to be a useful tool for verifying this. Furthermore, we have highlighted the difference between the LOS power factor and the Rician K-factor and support this assertion with the measured data from a Rician fading channel. We show that the DOA spectrum noticeably depends on the DOD. Using the ergodic channel capacity as a metric, we have compared the performance of the Kronecker, VCR, and Weichselberger models for the outdoor-to-indoor scenario. The Kronecker model is not applicable in our case due to the breakdown of the DOA–DOD decoupling assumptions; this holds true even for the NLOS scenarios. Compared to the VCR model, the Weichselberger model provides a better fit to the measured capacity for both the LOS and NLOS scenarios.

Our results can serve as a basis for understanding the outdoor-to-indoor MIMO channels and have served as an input to the COST 273 MIMO channel model [32].

ACKNOWLEDGMENT

The authors would like to thank Prof. L. Greenstein, Prof. E. Bonek, and members of the COST 273 subworking group 2.1 for fruitful discussions regarding the Rician K-factor; the informative input from Dr. A. Sayeed regarding the generalization of the VCR to UCAs; and TU Ilmenau, Ilmenau, Germany, for the loan of their antenna arrays.

REFERENCES

[1] J. H. Winters, "On the capacity of radio communications systems with diversity in Rayleigh fading environments," *IEEE J. Sel. Areas Commun.*, vol. SAC-5, no. 5, pp. 871–878, Jun. 1987.

[2] G. J. Foschini and M. J. Gans, "On limits of wireless communications in a fading environment when using multiple antennas," *Wirel. Pers. Commun.*, vol. 6, no. 3, pp. 311–335, Mar. 1998.

[3] M. Steinbauer, A. F. Molisch, and E. Bonek, "The double-directional radio channel," *IEEE Antennas Propag. Mag.*, vol. 43, no. 4, pp. 51–63, Aug. 2001.

[4] D. Chizhik, J. Ling, P. W. Wolniansky, R. A. Valenzuela, N. Costa, and K. Huber, "Multiple-input-multiple-output measurements and modeling in Manhattan," *IEEE J. Sel. Areas Commun.*, vol. 21, no. 3, pp. 321–331, Apr. 2003.

[5] R. Thomä, D. Hampicke, M. Landmann, G. Sommerkorn, and A. Richter, "MIMO measurement for double-directional channel modelling," in *Proc. IEE Semin. MIMO: Commun. Syst. From Concept to Implementations (Ref. No. 2001/175)*, Dec. 2001, pp. 1/1–1/7.

[6] K. Yu, M. Bengtsson, B. Ottersten, D. McNamara, P. Karlsson, and M. Beach, "Second order statistics of NLOS indoor MIMO channels based on 5.2 GHz measurements," in *Proc. IEEE Globecom*, 2001, vol. 1, pp. 156–160.

[7] W. Weichselberger, M. Herdin, H. Özcelik, and E. Bonek, "A stochastic MIMO channel model with joint correlation of both link ends," *IEEE Trans. Wireless Commun.*, vol. 5, no. 1, pp. 90–100, Jan. 2006.

[8] S. Wyne, P. Almers, G. Eriksson, J. Karedal, F. Tufvesson, and A. F. Molisch, "Outdoor to indoor office MIMO measurements at 5.2 GHz," in *Proc. IEEE VTC—Fall*, Los Angeles, CA, 2004, pp. 101–105.

[9] J. Medbo, F. Harrysson, H. Asplund, and J. E. Berg, "Measurements and analysis of a MIMO macrocell outdoor–indoor scenario at 1947 MHz," in *Proc. IEEE VTC—Spring*, 2004, vol. 1, pp. 261–265.

[10] H. T. Nguyen, J. B. Andersen, and G. F. Pedersen, "Characterization of the indoor/outdoor to indoor MIMO radio channel at 2.140 GHz," *Wirel. Pers. Commun.*, vol. 35, no. 3, pp. 289–309, Nov. 2005.

[11] D. Gesbert, H. Bolcskei, D. A. Gore, and A. J. Paulraj, "Outdoor MIMO wireless channels: Models and performance prediction," *IEEE Trans. Commun.*, vol. 50, no. 12, pp. 1926–1934, Dec. 2002.

[12] P. Almers, F. Tufvesson, and A. F. Molisch, "Keyhole effect in MIMO wireless channels: Measurements and theory," *IEEE Trans. Wireless Commun.*, vol. 5, no. 12, pp. 3596–3604, Dec. 2006.

[13] J. P. Kermoal, L. Schumacher, K. I. Pedersen, P. E. Mogensen, and F. Frederiksen, "A stochastic MIMO radio channel model with experimental validation," *IEEE J. Sel. Areas Commun.*, vol. 20, no. 6, pp. 1211–1226, Aug. 2002.

[14] H. Özcelik, N. Czink, and E. Bonek, "What makes a good MIMO channel model," in *Proc. IEEE VTC—Spring*, Stockholm, Sweden, May/Jun. 2005, pp. 156–160.

[15] S. Wyne, A. F. Molisch, P. Almers, G. Eriksson, J. Karedal, and F. Tufvesson, "Statistical evaluation of outdoor-to-indoor office MIMO measurements at 5.2 GHz," in *Proc. IEEE VTC—Spring*, Stockholm, Sweden, 2005, pp. 146–150.

[16] [Online]. Available: http://www.channelsounder.de

[17] B. H. Fleury, M. Tschudin, R. Heddergott, D. Dahlhaus, and K. Pedersen, "Channel parameter estimation in mobile radio environments using the SAGE algorithm," *IEEE J. Sel. Areas Commun.*, vol. 17, no. 3, pp. 434–450, Mar. 1999.

[18] A. F. Molisch, *Wireless Communications*. Piscataway, NJ: IEEE Press–Wiley, 2005.

[19] J. Medbo, M. Riback, H. Asplund, and J. Berg, "MIMO channel characteristics in a small macrocell measured at 5.25 GHz and 200 MHz bandwidth," in *Proc. IEEE VTC—Fall*, 2005, vol. 1, pp. 372–376.

[20] B. H. Fleury, "First- and second-order characterization of direction dispersion and space selectivity in the radio channel," *IEEE Trans. Inf. Theory*, vol. 46, no. 6, pp. 2027–2044, Sep. 2000.

[21] P. A. Bello, "Characterization of randomly time-variant linear channels," *IEEE Trans. Commun.*, vol. COM-11, no. 4, pp. 360–393, Dec. 1963.

[22] S. Wyne, N. Czink, J. Karedal, P. Almers, F. Tufvesson, and A. F. Molisch, "A cluster-based analysis of outdoor-to-indoor office MIMO measurements at 5.2 GHz," in *Proc. IEEE VTC—Fall*, Montreal, QC, Canada, 2006, pp. 1–5.

[23] P. Soma, D. S. Baum, V. Erceg, R. Krishnamoorthy, and A. J. Paulraj, "Analysis and modeling of multiple-input multiple-output (MIMO) radio channel based on outdoor measurements conducted at 2.5 GHz for fixed BWA applications," in *Proc. IEEE ICC*, 2002, vol. 1, pp. 272–276.

[24] E. W. Stacy, "A generalisation of the Gamma function," *Ann. Math. Stat.*, vol. 33, pp. 1187–1192, 1962.

[25] J. Griffiths and J. McGeehan, "Interrelationship between some statistical distributions used in radio wave propagation," *Proc. Inst. Electr. Eng.—F*, vol. 129, no. 6, pp. 411–417, Dec. 1982.

[26] R. Vaughan and J. B. Andersen, *Channels, Propagation and Antennas for Mobile Communications*, 1st ed. London, U.K.: IEE, 2003.

[27] M. Abramowitz and I. Stegun, *Handbook of Mathematical Functions*. New York: Dover, 1966.

[28] A. J. Coulson, A. G. Williamson, and R. G. Vaughan, "Improved fading distribution for mobile radio," *Proc. Inst. Electr. Eng.—Commun.*, vol. 145, no. 3, pp. 197–202, Jun. 1998.

[29] L. J. Greenstein, D. G. Michelson, and V. Erceg, "Moment-method estimation of the Ricean K-factor," *IEEE Commun. Lett.*, vol. 3, no. 6, pp. 175–176, Jun. 1999.

[30] M. A. Jensen and J. Wallace, "A review of antennas and propagation for MIMO wireless communications," *IEEE Trans. Antennas Propag.*, vol. 52, no. 11, pp. 2810–2824, Nov. 2004.

[31] A. M. Sayeed, "Deconstructing multiantenna fading channels," *IEEE Trans. Signal Process.*, vol. 50, no. 10, pp. 2563–2579, Oct. 2002.

[32] *COST 273 Final Report: Towards Mobile Broadband Multimedia Networks*, L. Correia, Ed. Amsterdam, The Netherlands: Elsevier, 2006.

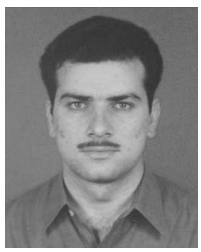

Shurjeel Wyne (S'03) received the B.Sc. degree in electrical engineering from the University of Engineering and Technology (UET) Lahore, Lahore, Pakistan, and the M.S. degree in digital communications from Chalmers University of Technology, Göteborg, Sweden. In 2003, he joined Lund University, Lund, Sweden, where he is working towards the Ph.D. degree with the Department of Electrical and Information Technology.

His research interests are in the field of measurement and modeling of wireless propagation channels, particularly for MIMO systems. He has participated in the European research initiatives "COST 273" and the European network of excellence "NEWCOM."

Andreas F. Molisch (S'89–M'95–SM'00–F'05) received the Dipl.Ing., Dr. Techn., and Habilitation degrees from the Technical University Vienna (TU Vienna), Vienna, Austria, in 1990, 1994, and 1999, respectively.

From 1991 to 2000, he was with TU Vienna, where he became an Associate Professor in 1999. From 2000 to 2002, he was with the Wireless Systems Research Department, AT&T (Bell) Laboratories Research, Middletown, NJ. Since 2002, he has been with Mitsubishi Electric Research Laboratories, Cambridge, MA, where he is currently a Distinguished Member of Technical Staff. He is also a Professor and a chair holder for radio systems with Lund University, Lund, Sweden. He has participated in the European research initiatives "COST 231," "COST 259," and "COST 273," where he was the Chairman of the MIMO Channel Working Group, the IEEE 802.15.4a Channel Model Standardization Group, and Commission C (signals and systems) of the International Union of Radio Scientists (URSI). He has authored, coauthored, or edited four books, among them, the recent textbook *Wireless Communications* (Wiley-IEEE Press), 11 book chapters, some 100 journal papers, and numerous conference contributions. He has done research in the areas of SAW filters, radiative transfer in atomic vapors, atomic line filters, smart antennas, and wideband systems. His current research interests are the measurement and modeling of mobile radio channels, UWB, cooperative communications, and MIMO systems.

Dr. Molisch is an IEEE Distinguished Lecturer and the recipient of several awards. He is an Editor of the IEEE TRANSACTIONS ON WIRELESS COMMUNICATIONS and a Co-Editor of recent and upcoming special issues on UWB (in the IEEE JOURNAL ON SELECTED AREAS IN COMMUNICATIONS and the PROCEEDINGS OF THE IEEE). He has been a member of numerous Technical Program Committees (TPCs), e.g., Vice Chair of the TPC of the Vehicular Technology Conference (VTC) 2005 Spring, General Chair of the International Conference on Ultra-Wideband (ICUWB) 2006, and TPC Cochair of the wireless symposium of Globecom 2007.

Peter Almers received the M.S. degree in electrical engineering and the Ph.D. degree in radio systems from Lund University, Lund, Sweden, in 1998 and 2007, respectively.

In 1998, he was with the Radio Research Department, TeliaSonera AB (formerly Telia AB), Malmö, Sweden, where he mainly worked with WCDMA physical layer issues and 3GPP WG1 standardization. In 2001, he was with the Radio Systems Group, Lunds Tekniska Högskola (LTH), Lund University, as a Ph.D. student (50% funded by TeliaSonera AB). He has participated in the European research initiative COST 273 and the European network of excellence NEWCOM and is currently involved in the NORDITE project WILATI. He is currently a Research Fellow with the Department of Electrical and Information Technology, Lund University.

Dr. Almers received the IEEE Best Student Paper Award at the 2002 International Symposium on Personal, Indoor, and Mobile Radio Communications.

Gunnar Eriksson received the M.S. degree in applied physics and electrical engineering from Linkoping University, Linköping, Sweden, in 1987. He is currently working toward the Ph.D. degree with the Department of Electrical and Information Technology, Lund University, Lund, Sweden.

Since 1987, he has been with the Department of Communication Systems, Swedish Defence Research Agency (FOI), Linköping, where he is mainly working with channel characterization, modeling, and prediction of radio-wave propagation for the assessment of communication and radar systems performance within a wide range of the radio frequency spectrum. His current research interests are mainly in the field of channel measurements and modeling for MIMO systems, particularly for peer-to-peer systems and with a focus on frequencies in the low UHF region.

Johan Karedal (S'04) received the M.S. degree in engineering physics in 2002 from Lund University, Lund, Sweden, where he is currently working toward the Ph.D. degree with the Department of Electrical and Information Technology.

His research interests include channel measurement and modeling for MIMO and UWB systems. He has participated in the European research initiative "MAGNET."

Fredrik Tufvesson (S'97–A'00–M'04–SM'07) was born in Lund, Sweden, in 1970. He received the M.S. degree in electrical engineering, the Licentiate degree, and the Ph.D. degree from Lund University, in 1994, 1998, and 2000, respectively.

After almost two years at a startup company (Fiberless Society), he is currently an Associate Professor with the Department of Electrical and Information Technology, Lund University. His main research interests are channel measurements and modeling for wireless communication, including channels for both MIMO and UWB systems. In addition, he also works with channel estimation and synchronization problems, OFDM system design, and UWB transceiver design.